

A Dissipative Systems Theory for FDTD with Application to Stability Analysis and Subgridding

Fadime Bekmambetova, Xinyue Zhang, and Piero Triverio, *Senior Member, IEEE*

Abstract—This paper establishes a far-reaching connection between the Finite-Difference Time-Domain method (FDTD) and the theory of dissipative systems. The FDTD equations for a rectangular region are written as a dynamical system having the magnetic and electric fields on the boundary as inputs and outputs. Suitable expressions for the energy stored in the region and the energy absorbed from the boundaries are introduced, and used to show that the FDTD system is dissipative under a generalized Courant-Friedrichs-Lewy condition. Based on the concept of dissipation, a powerful theoretical framework to investigate the stability of FDTD methods is devised. The new method makes FDTD stability proofs simpler, more intuitive, and modular. Stability conditions can indeed be given on the individual components (e.g. boundary conditions, meshes, embedded models) instead of the whole coupled setup. As an example of application, we derive a new subgridding method with material traverse, arbitrary grid refinement, and guaranteed stability. The method is easy to implement and has a straightforward stability proof. Numerical results confirm its stability, low reflections, and ability to handle material traverse.

Index Terms—finite-difference time-domain, stability, energy, dissipation, subgridding.

I. INTRODUCTION

The Finite-Difference Time-Domain (FDTD) method is widely used to solve Maxwell's equations numerically in microwave and antenna engineering, photonics and physics [1], [2]. FDTD is versatile, easy to implement, and has a low computational cost per time step. Through explicit update equations, FDTD recursively computes the electric and magnetic field in the region of interest without requiring the solution of linear systems. This update process is stable if time step Δt satisfies the Courant-Friedrichs-Lewy (CFL) stability limit [2]

$$\Delta t < \frac{1}{\sqrt{\frac{1}{\varepsilon\mu} \sqrt{\frac{1}{\Delta x^2} + \frac{1}{\Delta y^2} + \frac{1}{\Delta z^2}}}}, \quad (1)$$

where Δx , Δy , Δz denote cell size, ε denotes permittivity and μ denotes permeability. While many breakthroughs have been achieved in FDTD since Yee's original algorithm [3], the efficiency of FDTD for multiscale problems remains an open problem. The simultaneous presence of large and small geometrical features can dramatically reduce FDTD efficiency

because of two factors. First, the mesh has to be refined, at least locally, to properly resolve small features, which increases the number of unknowns and the cost per iteration. Second, because of (1), a mesh refinement imposes a smaller time step, which further increases computational cost. For example, a 3X refinement of the entire FDTD mesh increases computational cost by 81 times. These issues are unfortunate since multiscale problems abound in practice.

Numerous solutions have been proposed to mitigate this issue, including sophisticated boundary conditions to mimic open spaces [2], local grid refinement [4], [5], [6] (commonly known as *subgridding*), thin wire models [1], lumped elements [7], [8], and hybridizations with model order reduction [9], [10], [11], finite elements [12], integral equations [13], ray tracing [14] and implicit schemes like ADI-FDTD [15], [16]. From a system theory viewpoint, many of these methods consist of the interconnection of *subsystems*, such as models, algorithms, boundary conditions. For example, in [13], an FDTD model, used to describe an inhomogeneous scatterer, is coupled to the time-domain method of moments, used to model a thin-wire antenna. In this way, one can leverage the respective strengths of different algorithms. However, while the stability properties of the individual algorithms may be well understood, ensuring the stability of their combination can be a formidable task. Ensuring stability is not trivial even in the relatively simple case of FDTD subgridding, where one just couples a coarse and a fine FDTD grid through an interpolation rule to relate fields at the grid transition. The lack of a systematic approach to ensure the stability of advanced FDTD methods is a major issue, that limits the development of new methods and their adoption by industry, where guaranteed stability is mandatory. This issue is the main motivation for this paper, that proposes a new theoretical framework to investigate and ensure the stability of both simple and advanced FDTD methods.

Several techniques are available to analyze the stability of FDTD-like methods. Von Neumann analysis [1] is the simplest, but is only applicable to uniform meshes and homogeneous materials. The iteration method [2] checks if the eigenvalues of the matrix that relates the current and next field solution are all below one in magnitude. In the energy method [8] instead, one writes an expression for the total energy stored in the simulation domain, and then checks if the algorithm satisfies a discrete equivalent of the principle of energy conservation. Since energy conservation prevents an unphysical growth of the solution, this implies stability [17]. The iteration and energy methods are general, but they can lead to long derivations, since they require the analysis of the whole

Manuscript received ...; revised ...

This work was supported in part by the Natural Sciences and Engineering Research Council of Canada (Discovery grant program) and in part by the Canada Research Chairs program.

F. Bekmambetova, X. Zhang and P. Triverio are with the Edward S. Rogers Sr. Department of Electrical and Computer Engineering, University of Toronto, Toronto, M5S 3G4 Canada (email: fadime.bekmambetova@mail.utoronto.ca, xinyue.zhang.zhang@mail.utoronto.ca, piero.triverio@utoronto.ca).

coupled scheme, which may consist of many subsystems such as FDTD meshes, different boundary conditions, reduced order models, and so on. For example, in a subgridding scenario, one must derive the iteration matrix or energy function of the whole scheme, taking simultaneously into account coarse and fine meshes, interpolation rules and boundary conditions. This issue makes stability analysis quite involved. Moreover, it does not yield stability conditions on the individual subsystems. Consequently, if a subsystem is changed (for example, a different boundary condition is introduced), the iteration matrix or energy function of the whole problem must be derived again.

In this paper, we propose a new stability framework for FDTD. The framework is based on the theory of dissipative systems [18], and generalizes the energy method. First, starting from FDTD update equations, we develop a self-contained mathematical model for a region with arbitrary permittivity, permeability and conductivity. The model is in the form of a discrete time dynamical system. The magnetic field tangential to the boundary is taken as input, while the electric field tangential to the boundary is taken as output. Through this form, we reveal that an FDTD model can be interpreted as a dynamical system which is dissipative when Δt satisfies a generalized CFL condition. If this condition is not met, the system can generate energy on its own, leading to an unstable simulation. We thus establish a connection between FDTD and the elegant theory of dissipative systems, which is a novel result. We believe that this connection will greatly benefit the FDTD community, since the theory of dissipative systems has been extremely successful in control theory for ensuring the stability of interconnected systems. This key result sets the basis for a powerful FDTD stability theory, where each part of a given FDTD setup (standard meshes, boundary conditions, interpolation schemes, ...) is interpreted as a subsystem, and is required to be dissipative. Since the connection of dissipative systems is dissipative [18], [17], this will ensure the stability of the FDTD algorithm resulting from the connection of the subsystems. The proposed theory has numerous advantages. It simplifies stability proofs, since conditions can be imposed on *each subsystem individually*, rather than on the whole coupled algorithm. Stability proofs are thus made modular and “reusable”: once a given FDTD model (e.g., an advanced boundary condition) has been deemed to be dissipative, it can be combined to any other dissipative FDTD subsystem with guaranteed stability. The proposed approach also naturally provides the CFL stability limit of the resulting scheme, which will be the most restrictive CFL limit of the individual subsystems. Finally, the theory is intuitive, since it is based on the concept of energy, familiar to most scientists. The proposed theory is presented in 2D, for the sake of clarity. An extension to 3D is feasible and is currently under development.

As an example of application, the proposed theory is used to derive the subgridding algorithm which is stable by construction, and has several desirable features. Material traverse is supported for both dielectrics and highly conductive materials, which is a limitation of other stable subgridding methods [19]. The proposed method has low reflections, and avoids non-rectangular cells [6], finite element concepts [20] and Withney forms [21], [22]. Corners are natively supported

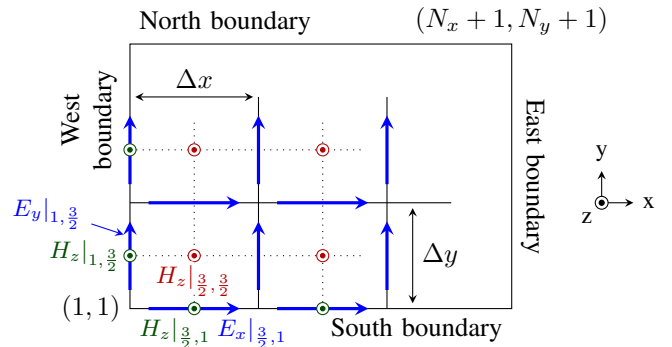


Figure 1: Graphical representation of the 2D region considered in Sec. II. The hanging variables introduced on the four boundaries are denoted in green.

without any special treatment [5] nor L-shaped cells [6]. Ultimately, the proposed algorithm just consists of a compact FDTD-like update equation for the edges between coarse and fine mesh, and is thus easy to implement. This update equation is provided explicitly for an arbitrary integer refinement ratio r , while several previous works [5], [6] provide the update weights only for specific refinements (typically $r = 2$ or 3), leaving the derivation of other cases to the Reader.

The paper is organized as follows. In Sec. II, we cast the FDTD update equations for a rectangular region into the form of a dynamical system with suitable inputs and outputs. In Sec. III, we show that FDTD equations can be interpreted as a dissipative system, and propose the new stability theory. The theory is applied to derive a stable subgridding algorithm in Sec. IV, followed by numerical results in Sec. V.

II. DISCRETE TIME DYNAMICAL MODEL FOR A 2D FDTD REGION

The goal of this section is to cast the FDTD equations for a 2D region into the form of a discrete time dynamical model. The model shall be self-contained, involving only field samples from the nodes belonging to the region. This goal will be achieved by introducing suitable magnetic field samples at the boundaries.

We consider the 2D rectangular region shown in Fig. 1, operating in a TE mode with components E_x , E_y , and H_z . The region is discretized with a uniform rectangular grid with $N_x \times N_y$ cells, of width Δx and height Δy . In addition to the field samples used by standard FDTD, we also sample the H field on the four boundaries of the region. These additional samples will be referred to as *hanging variables* [22], and will allow us to:

- 1) develop a self-contained model for the region, which does not involve field samples beyond its boundaries;
- 2) derive an expression for the energy absorbed from each boundary;
- 3) connect the FDTD grid to other subsystems while maintaining stability.

To keep the notation compact, we collect all E_x and E_y samples into column vectors \mathbf{E}_x^n and \mathbf{E}_y^n , of size $N_{E_x} = N_x(N_y + 1)$ and $N_{E_y} = (N_x + 1)N_y$, respectively. The H_z

samples at the internal nodes are collected into column vector $\mathbf{H}_z^{n+\frac{1}{2}}$ of size $N_{H_z} = N_x N_y$. The hanging variables on the South boundary of the region are collected into the $N_x \times 1$ vector

$$\mathbf{H}_S^{n+\frac{1}{2}} = \left[H_z|_{1+\frac{1}{2},1}^{n+\frac{1}{2}} \quad \dots \quad H_z|_{N_x+\frac{1}{2},1}^{n+\frac{1}{2}} \right]^T. \quad (2)$$

Similarly, the hanging variables on the North, East and West sides are cast into column vectors $\mathbf{H}_N^{n+\frac{1}{2}}$, $\mathbf{H}_E^{n+\frac{1}{2}}$ and $\mathbf{H}_W^{n+\frac{1}{2}}$, respectively.

A. State Equation for Each Node

The dynamical model for the region consists of an update equation for each E and H sample, excluding the hanging variables. Those variables will indeed be eliminated once the region is connected to the surrounding subsystems or to some boundary conditions.

1) *Internal H_z Nodes:* For these nodes, we use a standard FDTD update [2]

$$\begin{aligned} \Delta x \Delta y \frac{\mu}{\Delta t} H_z|_{i+\frac{1}{2},j+\frac{1}{2}}^{n+\frac{1}{2}} &= \Delta x \Delta y \frac{\mu}{\Delta t} H_z|_{i+\frac{1}{2},j+\frac{1}{2}}^{n-\frac{1}{2}} \\ &\quad - \Delta x E_x|_{i+\frac{1}{2},j}^n + \Delta x E_x|_{i+\frac{1}{2},j+1}^n \\ &\quad + \Delta y E_y|_{i,j+\frac{1}{2}}^n - \Delta y E_y|_{i+1,j+\frac{1}{2}}^n \end{aligned} \quad (3)$$

for $i = 1, \dots, N_x$ and $j = 1, \dots, N_y$. In (3), μ denotes the average permittivity on the edge where $H_z|_{i+\frac{1}{2},j+\frac{1}{2}}^{n+\frac{1}{2}}$ is sampled. Subscripts are omitted from μ in order to simplify the notation. Equations (3) can be written in matrix form as

$$\mathbf{D}_A \frac{\mathbf{D}_\mu}{\Delta t} \mathbf{H}_z^{n+\frac{1}{2}} = \mathbf{D}_A \frac{\mathbf{D}_\mu}{\Delta t} \mathbf{H}_z^{n-\frac{1}{2}} + \mathbf{G}_y \mathbf{D}_{l_x} \mathbf{E}_x^n - \mathbf{G}_x \mathbf{D}_{l_y} \mathbf{E}_y^n, \quad (4)$$

where \mathbf{D}_A is a diagonal matrix containing the area of the primary cells, \mathbf{D}_μ is a diagonal matrix containing the average permittivity on each edge of the secondary grid. Diagonal matrices

$$\mathbf{D}_{l_x} = \Delta x \mathbf{I}_{N_{E_x}} \quad \mathbf{D}_{l_y} = \Delta y \mathbf{I}_{N_{E_y}} \quad (5)$$

contain the length of the x - and y -directed edges of the primary grid, respectively. With \mathbf{I}_m , we denote the $m \times m$ identity matrix. Matrix \mathbf{G}_x is the discrete derivative operator along x , which can be written as

$$\mathbf{G}_x = \mathbf{I}_{N_y} \otimes \mathbf{W}_{N_x}, \quad (6)$$

where \otimes is the Kronecker's product [23] and \mathbf{W}_{N_x} is the $N_x \times (N_x + 1)$ matrix [24]

$$\mathbf{W}_n = \begin{bmatrix} -1 & +1 & & & & \\ & -1 & +1 & & & \\ & & & \ddots & \ddots & \\ & & & & -1 & +1 \end{bmatrix}. \quad (7)$$

Similarly,

$$\mathbf{G}_y = \mathbf{W}_{N_y} \otimes \mathbf{I}_{N_x}. \quad (8)$$

2) *E_x Nodes:* For the E_x nodes that fall strictly inside the region, we use a standard FDTD update [2]

$$\begin{aligned} \Delta x \Delta y \left(\frac{\varepsilon_x}{\Delta t} + \frac{\sigma_x}{2} \right) E_x|_{i+\frac{1}{2},j}^{n+1} &= \Delta x \Delta y \left(\frac{\varepsilon_x}{\Delta t} - \frac{\sigma_x}{2} \right) E_x|_{i+\frac{1}{2},j}^n \\ &\quad + \Delta x H_z|_{i+\frac{1}{2},j+\frac{1}{2}}^{n+\frac{1}{2}} - \Delta x H_z|_{i+\frac{1}{2},j-\frac{1}{2}}^{n+\frac{1}{2}} \end{aligned} \quad (9)$$

for $i = 1, \dots, N_x$ and $j = 2, \dots, N_y$. In (9), ε_x and σ_x denote, respectively, the average permittivity and average conductivity on the corresponding edge. While the common factor Δx could be eliminated from (9), it is kept as it will be useful later.

For the E_x nodes on the South boundary, the standard FDTD update equation involves a H_z sample outside the region. In order to avoid this, we apply the finite difference approximation to the half step of the secondary grid between nodes $(i + \frac{1}{2}, 1 + \frac{1}{2})$ and $(i + \frac{1}{2}, 1)$, making use of the hanging variables. In this way, we obtain an update equation that involves only field samples from the considered region

$$\begin{aligned} \Delta x \frac{\Delta y}{2} \left(\frac{\varepsilon_x}{\Delta t} + \frac{\sigma_x}{2} \right) E_x|_{i+\frac{1}{2},1}^{n+1} &= \\ \Delta x \frac{\Delta y}{2} \left(\frac{\varepsilon_x}{\Delta t} - \frac{\sigma_x}{2} \right) E_x|_{i+\frac{1}{2},1}^n & \\ + \Delta x H_z|_{i+\frac{1}{2},1+\frac{1}{2}}^{n+\frac{1}{2}} - \Delta x H_z|_{i+\frac{1}{2},1}^{n+\frac{1}{2}}, & \end{aligned} \quad (10)$$

for $i = 1, \dots, N_x$. In (10), ε_x and σ_x denote the material properties of the half cell between nodes $(i + \frac{1}{2}, 1 + \frac{1}{2})$ and $(i + \frac{1}{2}, 1)$. The update equation for the E_x nodes on the North boundary is obtained similarly, and reads

$$\begin{aligned} \Delta x \frac{\Delta y}{2} \left(\frac{\varepsilon_x}{\Delta t} + \frac{\sigma_x}{2} \right) E_x|_{i+\frac{1}{2},N_y+1}^{n+1} &= \\ \Delta x \frac{\Delta y}{2} \left(\frac{\varepsilon_x}{\Delta t} - \frac{\sigma_x}{2} \right) E_x|_{i+\frac{1}{2},N_y+1}^n & \\ + \Delta x H_z|_{i+\frac{1}{2},N_y+1}^{n+\frac{1}{2}} - \Delta x H_z|_{i+\frac{1}{2},N_y+\frac{1}{2}}^{n+\frac{1}{2}}, & \end{aligned} \quad (11)$$

for $i = 1, \dots, N_x$. Relations (9), (10) and (11) can be compactly written as

$$\begin{aligned} \mathbf{D}_{l_x} \mathbf{D}_{l_y}' \left(\frac{\mathbf{D}_{\varepsilon_x}}{\Delta t} + \frac{\mathbf{D}_{\sigma_x}}{2} \right) \mathbf{E}_x^{n+1} &= \\ \mathbf{D}_{l_x} \mathbf{D}_{l_y}' \left(\frac{\mathbf{D}_{\varepsilon_x}}{\Delta t} - \frac{\mathbf{D}_{\sigma_x}}{2} \right) \mathbf{E}_x^n - \mathbf{D}_{l_x} \mathbf{G}_y^T \mathbf{H}_z^{n+\frac{1}{2}} & \\ + [\mathbf{D}_{l_x} \mathbf{B}_S \quad \mathbf{D}_{l_x} \mathbf{B}_N] \begin{bmatrix} \mathbf{H}_S^{n+\frac{1}{2}} \\ \mathbf{H}_N^{n+\frac{1}{2}} \end{bmatrix}, & \end{aligned} \quad (12)$$

where

- \mathbf{D}_{l_y}' is an $N_{E_x} \times N_{E_x}$ diagonal matrix containing the length of the y -directed edges of the secondary grid, including the half-edges of length $\Delta y/2$ that intersect the North and South boundaries;
- $\mathbf{D}_{\varepsilon_x}$ and \mathbf{D}_{σ_x} are diagonal matrices storing the permittivity and conductivity on each x -directed primary edge, respectively;
- \mathbf{B}_S has all entries set to zero, except for a -1 at the intersection of each row associated with a South boundary edge and the column of the corresponding hanging variable in $\mathbf{H}_S^{n+\frac{1}{2}}$;

- \mathbf{B}_N is defined similarly to \mathbf{B}_S , but has a +1 on each entry associated with an edge of the North boundary.

3) E_y Nodes: The update equations for the E_y nodes are derived with a similar procedure. A standard FDTD update equation is written for the E_y nodes that fall strictly inside the region. For the E_y nodes on the West and East boundaries, instead, finite differences are applied on a half grid step, similarly to (10) and (11). This process leads to

$$\begin{aligned} \mathbf{D}_{l_y} \mathbf{D}_{l'_x} \left(\frac{\mathbf{D}_{\varepsilon_y}}{\Delta t} + \frac{\mathbf{D}_{\sigma_y}}{2} \right) \mathbf{E}_y^{n+1} = \\ \mathbf{D}_{l_y} \mathbf{D}_{l'_x} \left(\frac{\mathbf{D}_{\varepsilon_y}}{\Delta t} - \frac{\mathbf{D}_{\sigma_y}}{2} \right) \mathbf{E}_y^n + \mathbf{D}_{l_y} \mathbf{G}_x^T \mathbf{H}_z^{n+\frac{1}{2}} \\ + [\mathbf{D}_{l_y} \mathbf{B}_W \quad \mathbf{D}_{l_y} \mathbf{B}_E] \begin{bmatrix} \mathbf{H}_W^{n+\frac{1}{2}} \\ \mathbf{H}_E^{n+\frac{1}{2}} \end{bmatrix}, \end{aligned} \quad (13)$$

where

- $\mathbf{D}_{l'_x}$ is an $N_{E_y} \times N_{E_y}$ diagonal matrix containing the length of the x -directed edges of the secondary grid, including the half-edges of length $\Delta x/2$ that intersect the East and West boundaries;
- $\mathbf{D}_{\varepsilon_y}$ and \mathbf{D}_{σ_y} are diagonal permittivity and conductivity matrices associated with the y -directed edges of the primary grid, respectively;
- \mathbf{B}_W has all entries set to zero, except for a +1 at the intersection of each row associated with a West boundary edge and the column of the corresponding hanging variable in $\mathbf{H}_W^{n+\frac{1}{2}}$;
- \mathbf{B}_E is analogous to \mathbf{B}_W , but has a -1 on each entry associated with an East boundary edge.

B. Descriptor System Formulation

The update equations derived in the previous sections form a complete dynamical model for the rectangular region

$$(\mathbf{R} + \mathbf{F})\mathbf{x}^{n+1} = (\mathbf{R} - \mathbf{F})\mathbf{x}^n + \mathbf{B}\mathbf{u}^{n+\frac{1}{2}}, \quad (14a)$$

$$\mathbf{y}^n = \mathbf{L}^T \mathbf{x}^n. \quad (14b)$$

The first equation (14a) is formed by update equations (4), (12) and (13), and updates the state vector

$$\mathbf{x}^n = \begin{bmatrix} \mathbf{E}_x^n \\ \mathbf{E}_y^n \\ \mathbf{H}_z^{n-\frac{1}{2}} \end{bmatrix}, \quad (15)$$

which consists of all electric and magnetic field samples in the region, excluding hanging variables. The input vector $\mathbf{u}^{n+\frac{1}{2}}$ and output vector \mathbf{y}^n are given by

$$\mathbf{u}^{n+\frac{1}{2}} = \begin{bmatrix} \mathbf{H}_S^{n+\frac{1}{2}} \\ \mathbf{H}_N^{n+\frac{1}{2}} \\ \mathbf{H}_W^{n+\frac{1}{2}} \\ \mathbf{H}_E^{n+\frac{1}{2}} \end{bmatrix} \quad \mathbf{y}^n = \begin{bmatrix} \mathbf{E}_S^n \\ \mathbf{E}_N^n \\ \mathbf{E}_W^n \\ \mathbf{E}_E^n \end{bmatrix}. \quad (16)$$

The input vector contains all hanging variables, i.e. all magnetic field samples on the region boundaries. The output vector is made by the E samples at the same nodes, which are collected into vectors \mathbf{E}_S^n , \mathbf{E}_N^n , \mathbf{E}_W^n and \mathbf{E}_E^n . Output

equation (14b) extracts these values from the state vector \mathbf{x}^n . The coefficients matrices in (14a) and (14b) read

$$\mathbf{R} = \begin{bmatrix} \mathbf{D}_{l_x} \mathbf{D}_{l'_y} \frac{\mathbf{D}_{\varepsilon_x}}{\Delta t} & \mathbf{0} & \frac{1}{2} \mathbf{D}_{l_x} \mathbf{G}_y^T \\ \mathbf{0} & \mathbf{D}_{l_y} \mathbf{D}_{l'_x} \frac{\mathbf{D}_{\varepsilon_y}}{\Delta t} & -\frac{1}{2} \mathbf{D}_{l_y} \mathbf{G}_x^T \\ \frac{1}{2} \mathbf{G}_y \mathbf{D}_{l_x} & -\frac{1}{2} \mathbf{G}_x \mathbf{D}_{l_y} & \mathbf{D}_A \frac{\mathbf{D}_{\mu}}{\Delta t} \end{bmatrix}, \quad (17)$$

$$\mathbf{F} = \begin{bmatrix} \mathbf{D}_{l_x} \mathbf{D}_{l'_y} \frac{\mathbf{D}_{\sigma_x}}{2} & \mathbf{0} & \frac{1}{2} \mathbf{D}_{l_x} \mathbf{G}_y^T \\ \mathbf{0} & \mathbf{D}_{l_y} \mathbf{D}_{l'_x} \frac{\mathbf{D}_{\sigma_y}}{2} & -\frac{1}{2} \mathbf{D}_{l_y} \mathbf{G}_x^T \\ -\frac{1}{2} \mathbf{G}_y \mathbf{D}_{l_x} & \frac{1}{2} \mathbf{G}_x \mathbf{D}_{l_y} & \mathbf{0} \end{bmatrix}, \quad (18)$$

$$\mathbf{B} = \begin{bmatrix} \mathbf{D}_{l_x} \mathbf{B}_S & \mathbf{D}_{l_x} \mathbf{B}_N & \mathbf{0} & \mathbf{0} \\ \mathbf{0} & \mathbf{0} & \mathbf{D}_{l_y} \mathbf{B}_W & \mathbf{D}_{l_y} \mathbf{B}_E \\ \mathbf{0} & \mathbf{0} & \mathbf{0} & \mathbf{0} \end{bmatrix}, \quad (19)$$

$$\mathbf{L} = \begin{bmatrix} -\mathbf{B}_S & \mathbf{B}_N & \mathbf{0} & \mathbf{0} \\ \mathbf{0} & \mathbf{0} & \mathbf{B}_W & -\mathbf{B}_E \\ \mathbf{0} & \mathbf{0} & \mathbf{0} & \mathbf{0} \end{bmatrix}. \quad (20)$$

Equations (14a)-(14b) define an FDTD-like model for a 2D lossy, source-free region, with possibly non-uniform permittivity and permeability. From a control perspective, this model is a discrete time descriptor system [25], also known as generalized state-space. From an electrical standpoint, the model is an impedance-type description of the region, because it gives the electric field tangential to the boundary in terms of the tangential magnetic field. In [24], a special case of the proposed representation was derived for a lossy region enclosed by PEC boundaries. The proposed developments generalize [24] in two directions:

- 1) the assumption of a PEC termination is removed. Suitable input-output variables are introduced in such a way that model (14a)-(14b) can be connected to other subsystems, such as different FDTD grids, boundary conditions, or reduced models;
- 2) the proposed formulation will allow us to prove, in the next section, that FDTD equations can be interpreted as a dissipative dynamical system.

III. FDTD AS A DISSIPATIVE DISCRETE TIME SYSTEM

In this section, we define suitable expressions for the energy stored in the 2D region and the energy absorbed from its four boundaries. These expressions are then used to derive the conditions under which system (14a)-(14b) is dissipative.

A. Dissipation Inequality

A discrete time system like (14a)-(14b) is dissipative when it satisfies the following condition [26].

Definition 1. *Dynamic system (14a)-(14b) is said to be dissipative with supply rate $s(\mathbf{y}^n, \mathbf{u}^{n+\frac{1}{2}})$ if there exists a nonnegative function $\mathcal{E}(\mathbf{x}^n)$ with $\mathcal{E}(0) = 0$, called storage function, such that*

$$\mathcal{E}(\mathbf{x}^{n+1}) - \mathcal{E}(\mathbf{x}^n) \leq s(\mathbf{y}^n, \mathbf{u}^{n+\frac{1}{2}}) \quad (21)$$

for all $\mathbf{u}^{n+\frac{1}{2}}$ and all n .

The storage function $\mathcal{E}(\mathbf{x}^n)$ can be interpreted as the energy stored in the system at time n , while the supply rate

$s(\mathbf{y}^n, \mathbf{u}^{n+\frac{1}{2}})$ is the energy absorbed by the system from its boundaries between time n and $n+1$. Clearly, only dissipative systems can satisfy the *dissipation inequality* (21). Indeed, their stored energy can increase between time n and $n+1$ by *at most* the energy absorbed from the outside world. If this limit is violated, the system is considered active, since it can generate energy on its own. For most practical systems, inequality (21) is satisfied strictly because of the presence of losses.

B. Storage Function and Supply Rate

For system (14a)-(14b), we choose as candidate storage function

$$\mathcal{E}(\mathbf{x}^n) = \frac{\Delta t}{2} (\mathbf{x}^n)^T \mathbf{R} \mathbf{x}^n, \quad (22)$$

and as supply rate

$$s(\mathbf{y}^n, \mathbf{u}^{n+\frac{1}{2}}) = \Delta t \frac{(\mathbf{y}^n + \mathbf{y}^{n+1})^T}{2} \mathbf{L}^T \mathbf{B} \mathbf{u}^{n+\frac{1}{2}}. \quad (23)$$

Before showing that these functions satisfy (21), we investigate their physical meaning. Substituting (17) into (22), we get

$$\begin{aligned} \mathcal{E}(\mathbf{x}^n) = & \frac{1}{2} (\mathbf{E}_x^n)^T \mathbf{D}_{l_x} \mathbf{D}_{l'_y} \mathbf{D}_{\varepsilon_x} \mathbf{E}_x^n \\ & + \frac{1}{2} (\mathbf{E}_y^n)^T \mathbf{D}_{l_y} \mathbf{D}_{l'_x} \mathbf{D}_{\varepsilon_y} \mathbf{E}_y^n \\ & + \frac{\Delta t}{2} \left[\mathbf{G}_y \mathbf{D}_{l_x} \mathbf{E}_x^n - \mathbf{G}_x \mathbf{D}_{l_y} \mathbf{E}_y^n + \mathbf{D}_A \frac{\mathbf{D}_\mu}{\Delta t} \mathbf{H}_z^{n-\frac{1}{2}} \right]. \end{aligned} \quad (24)$$

Since the term between square brackets is the right hand side of (4), we can reduce (24) to

$$\begin{aligned} \mathcal{E}(\mathbf{x}^n) = & \frac{1}{2} (\mathbf{E}_x^n)^T \mathbf{D}_{l_x} \mathbf{D}_{l'_y} \mathbf{D}_{\varepsilon_x} \mathbf{E}_x^n \\ & + \frac{1}{2} (\mathbf{E}_y^n)^T \mathbf{D}_{l_y} \mathbf{D}_{l'_x} \mathbf{D}_{\varepsilon_y} \mathbf{E}_y^n \\ & + \frac{1}{2} (\mathbf{H}_z^{n-\frac{1}{2}})^T \mathbf{D}_A \mathbf{D}_\mu \mathbf{H}_z^{n+\frac{1}{2}}. \end{aligned} \quad (25)$$

$$\int_A \left[\frac{1}{2} \varepsilon E_x^2(t) + \frac{1}{2} \varepsilon E_y^2(t) + \frac{1}{2} \mu H_z^2(t) \right] dA, \quad (26)$$

the continuous expression for the electromagnetic energy per unit height of a 2D TE mode in a region of area A . The first term of (25) is the energy stored in the x component of the electric field in the region. Indeed, the diagonal matrix $\mathbf{D}_{l_x} \mathbf{D}_{l'_y}$ is the area of the half cells around the E_x edges. Similarly, the second and third term in (25) represent the energy stored in the E_y and H_z components, respectively.

We now discuss the physical meaning of supply rate (23). Direct inspection reveals that

$$\mathbf{L}^T \mathbf{B} = \begin{bmatrix} -\Delta x \mathbf{I}_{N_x} & \mathbf{0} & \mathbf{0} & \mathbf{0} \\ \mathbf{0} & +\Delta x \mathbf{I}_{N_x} & \mathbf{0} & \mathbf{0} \\ \mathbf{0} & \mathbf{0} & +\Delta y \mathbf{I}_{N_y} & \mathbf{0} \\ \mathbf{0} & \mathbf{0} & \mathbf{0} & -\Delta y \mathbf{I}_{N_y} \end{bmatrix}. \quad (27)$$

Substituting (27) into (23), we obtain

$$\begin{aligned} s(\mathbf{y}^n, \mathbf{u}^{n+\frac{1}{2}}) = & -\Delta t \Delta x \frac{(\mathbf{E}_S^n + \mathbf{E}_S^{n+1})^T}{2} \mathbf{H}_S^{n+\frac{1}{2}} \\ & + \Delta t \Delta x \frac{(\mathbf{E}_N^n + \mathbf{E}_N^{n+1})^T}{2} \mathbf{H}_N^{n+\frac{1}{2}} + \Delta t \Delta y \frac{(\mathbf{E}_W^n + \mathbf{E}_W^{n+1})^T}{2} \mathbf{H}_W^{n+\frac{1}{2}} \\ & - \Delta t \Delta y \frac{(\mathbf{E}_E^n + \mathbf{E}_E^{n+1})^T}{2} \mathbf{H}_E^{n+\frac{1}{2}}, \end{aligned} \quad (28)$$

and see that the supply rate is the sum of the energy absorbed by the region from each boundary between time n and $n+1$. Signs in (28) are consistent with the direction of the Poynting vector on each boundary.

C. Dissipativity Conditions

Using the proposed storage function (22) and supply rate (23), we can derive simple dissipativity conditions on the coefficients matrices \mathbf{R} , \mathbf{F} , \mathbf{B} and \mathbf{L} in (14a)-(14b).

Theorem 1. *If*

$$\mathbf{R} = \mathbf{R}^T > \mathbf{0}, \quad (29a)$$

$$\mathbf{F} + \mathbf{F}^T \geq \mathbf{0}, \quad (29b)$$

$$\mathbf{B} = \mathbf{L} \mathbf{L}^T \mathbf{B}, \quad (29c)$$

then system (14a)-(14b) is dissipative according to Definition 1, with (22) as storage function and (23) as supply rate.

Proof. Condition (29a) makes storage function (22) nonnegative for all \mathbf{x}^n , as required by Definition 1. Next, we show that if (29b) and (29c) hold, the dissipation inequality (21) will hold as well. Substituting (22) and (23) into (21), we obtain

$$(\mathbf{x}^{n+1})^T \mathbf{R} \mathbf{x}^{n+1} - (\mathbf{x}^n)^T \mathbf{R} \mathbf{x}^n - (\mathbf{y}^n + \mathbf{y}^{n+1})^T \mathbf{L}^T \mathbf{B} \mathbf{u}^{n+\frac{1}{2}} \leq 0.$$

This inequality can be rewritten as

$$\begin{aligned} & (\mathbf{x}^{n+1})^T \mathbf{R} (\mathbf{x}^{n+1} - \mathbf{x}^n) + (\mathbf{x}^{n+1} - \mathbf{x}^n)^T \mathbf{R} \mathbf{x}^n \\ & - (\mathbf{y}^n + \mathbf{y}^{n+1})^T \mathbf{L}^T \mathbf{B} \mathbf{u}^{n+\frac{1}{2}} \leq 0 \end{aligned} \quad (30)$$

From (14a), we have that

$$\mathbf{R} (\mathbf{x}^{n+1} - \mathbf{x}^n) = -\mathbf{F} (\mathbf{x}^{n+1} + \mathbf{x}^n) - \mathbf{B} \mathbf{u}^{n+\frac{1}{2}} \quad (31)$$

Using (31), the terms $\mathbf{R} (\mathbf{x}^{n+1} - \mathbf{x}^n)$ and $(\mathbf{x}^{n+1} - \mathbf{x}^n)^T \mathbf{R}$ in (30) can be expressed in terms of \mathbf{F}

$$\begin{aligned} & -(\mathbf{x}^{n+1})^T \mathbf{F} (\mathbf{x}^{n+1} + \mathbf{x}^n) - (\mathbf{x}^{n+1} + \mathbf{x}^n)^T \mathbf{F} \mathbf{x}^n \\ & + (\mathbf{x}^{n+1})^T \mathbf{B} \mathbf{u}^{n+\frac{1}{2}} + (\mathbf{u}^{n+\frac{1}{2}})^T \mathbf{B}^T \mathbf{x}^n \\ & - (\mathbf{x}^n)^T \mathbf{L} \mathbf{L}^T \mathbf{B} \mathbf{u}^{n+\frac{1}{2}} - (\mathbf{x}^{n+1})^T \mathbf{L} \mathbf{L}^T \mathbf{B} \mathbf{u}^{n+\frac{1}{2}} \leq 0 \end{aligned} \quad (32)$$

Under (29c), we can finally rewrite (32) as

$$(\mathbf{x}^{n+1} + \mathbf{x}^n)^T (\mathbf{F} + \mathbf{F}^T) (\mathbf{x}^{n+1} + \mathbf{x}^n) \geq 0 \quad (33)$$

which is clearly satisfied if (29b) holds. \square

We now investigate the physical meaning of the three dissipativity conditions, starting from (29c), which can be directly verified by combining (27) and (20). This condition holds because the region inputs and outputs in (16) are sampled at the same nodes, and is reminiscent of a similar

relation which holds for linear circuits under the impedance representation [27]. Condition (29b) is related to losses, and reads

$$\mathbf{F} + \mathbf{F}^T = \begin{bmatrix} \mathbf{D}_{l_x} \mathbf{D}_{l'_y} \mathbf{D}_{\sigma_x} & \mathbf{0} & \mathbf{0} \\ \mathbf{0} & \mathbf{D}_{l_y} \mathbf{D}_{l'_x} \mathbf{D}_{\sigma_y} & \mathbf{0} \\ \mathbf{0} & \mathbf{0} & \mathbf{0} \end{bmatrix} \geq 0. \quad (34)$$

Since \mathbf{D}_{l_x} , \mathbf{D}_{l_y} , $\mathbf{D}_{l'_x}$ and $\mathbf{D}_{l'_y}$ are diagonal with positive elements only, (34) boils down to

$$\mathbf{D}_{\sigma_x} \geq 0, \quad (35)$$

$$\mathbf{D}_{\sigma_y} \geq 0. \quad (36)$$

As one may expect, the average conductivity on each primary edge must be non-negative in a dissipative system. Condition (29a) is the most interesting, and is a generalized CFL criterion. From (17), we see that $\mathbf{R} = \mathbf{R}^T$ by construction. With the Schur's complement [28], we can transform (29a) into

$$\mathbf{D}_{l_x} \mathbf{D}_{l'_y} \mathbf{D}_{\varepsilon_x} > 0, \quad (37)$$

$$\mathbf{D}_{l_y} \mathbf{D}_{l'_x} \mathbf{D}_{\varepsilon_y} > 0, \quad (38)$$

$$\mathbf{S} \mathbf{S}^T < \frac{4}{\Delta t^2} \mathbf{I}_{N_{Hz}}, \quad (39)$$

where

$$\mathbf{S} = \mathbf{D}_A^{-\frac{1}{2}} \mathbf{D}_\mu^{-\frac{1}{2}} \begin{bmatrix} \mathbf{G}_y \mathbf{D}_{l_x}^{\frac{1}{2}} \mathbf{D}_{l'_y}^{-\frac{1}{2}} \mathbf{D}_{\varepsilon_x}^{-\frac{1}{2}} & -\mathbf{G}_x \mathbf{D}_{l_y}^{\frac{1}{2}} \mathbf{D}_{l'_x}^{-\frac{1}{2}} \mathbf{D}_{\varepsilon_y}^{-\frac{1}{2}} \end{bmatrix}. \quad (40)$$

Inequalities (37) and (38) are clearly satisfied by construction. If we denote with s_k the singular values of (40), inequality (39) will hold if

$$\Delta t < \frac{2}{s_k} \quad \forall k. \quad (41)$$

This condition sets an upper bound on the FDTD time step, and is analogous to the generalized CFL constraint derived in [24] for an FDTD grid terminated on PEC boundaries. From (40), we indeed see that the time step upper limit depends on grid size, permittivity and permeability. Using a time step which violates (41) has two consequences. First, the discretization of Maxwell's equations leads to an active discrete time model, even if the real physical system has positive losses everywhere, and should therefore be dissipative. The numerical model is thus inconsistent with the actual physics. Second, being able to generate energy on its own, model (14a)-(14b) can lead to divergent transient simulations. Even when such model is connected to other dissipative subsystems, its ability to generate energy on its own can destabilize the whole simulation. The proposed theory provides a new, deeper understanding on the root causes of FDTD instability, and is able to pinpoint *which* part of an FDTD setup is responsible for it. It is hoped that this new explanation will facilitate the development of powerful FDTD schemes with guaranteed stability.

D. Relation to CFL Stability Limit

The relation between (41) and the CFL limit can be further understood if we apply (41) to a single cell. The purpose of (41) is to make storage function (22) non-negative. A

sufficient condition for this is to require the energy stored in *each* primary cell to be positive. This condition can be derived by applying (39) to a single primary cell. We consider the primary cell extending from node (i, j) to node $(i+1, j+1)$. The coefficient matrices for this special case can be obtained from the formulas in Sec. II by setting $N_x = N_y = 1$

$$\mathbf{D}_{l_x} = \Delta x \mathbf{I}_2 \quad \mathbf{D}_{l_y} = \Delta y \mathbf{I}_2 \quad (42)$$

$$\mathbf{D}_{l'_x} = \frac{\Delta x}{2} \mathbf{I}_2 \quad \mathbf{D}_{l'_y} = \frac{\Delta y}{2} \mathbf{I}_2 \quad (43)$$

$$\mathbf{G}_x = \mathbf{G}_y = [-1 \quad 1] \quad \mathbf{D}_A = \Delta x \Delta y \quad (44)$$

The permeability matrix $\mathbf{D}_\mu = \mu|_{i+\frac{1}{2}, j+\frac{1}{2}}$ is the average permeability on the secondary edge, while the permittivity matrices

$$\mathbf{D}_{\varepsilon_x} = \begin{bmatrix} \varepsilon_x|_{i+\frac{1}{2}, j} & 0 \\ 0 & \varepsilon_x|_{i+\frac{1}{2}, j+1} \end{bmatrix} \quad \mathbf{D}_{\varepsilon_y} = \begin{bmatrix} \varepsilon_y|_{i, j+\frac{1}{2}} & 0 \\ 0 & \varepsilon_y|_{i+1, j+\frac{1}{2}} \end{bmatrix} \quad (45)$$

contain the average permittivity on the four primary edges. Substituting (42)-(45) into (39), we obtain

$$\Delta t < \left[\frac{1}{2\Delta x^2 \mu|_{i+\frac{1}{2}, j+\frac{1}{2}}} \left(\frac{1}{\varepsilon_y|_{i, j+\frac{1}{2}}} + \frac{1}{\varepsilon_y|_{i+1, j+\frac{1}{2}}} \right) + \frac{1}{2\Delta y^2 \mu|_{i+\frac{1}{2}, j+\frac{1}{2}}} \left(\frac{1}{\varepsilon_x|_{i+\frac{1}{2}, j}} + \frac{1}{\varepsilon_x|_{i+\frac{1}{2}, j+1}} \right) \right]^{-\frac{1}{2}}, \quad (46)$$

which is a generalized CFL condition. For a uniform medium with permittivity ε and permeability μ , (46) reduces to

$$\Delta t < \frac{1}{\sqrt{\frac{1}{\varepsilon\mu}} \sqrt{\frac{1}{\Delta x^2} + \frac{1}{\Delta y^2}}}, \quad (47)$$

the CFL limit of 2D FDTD. This derivation confirms that (29a) is a generalized CFL condition, here reinterpreted in the context of dissipation.

E. Application to Stability Analysis

The proposed dissipation theory can be effectively used to investigate and enforce the stability of FDTD algorithms. Most FDTD setups consist of an interconnection of FDTD subsystems. In the simplest scenario, a uniform FDTD grid is connected to some boundary conditions. In most advanced scenarios, one may want to couple a main FDTD grid to refined grids, reduced models, lumped elements, or models from other numerical techniques, such as finite elements, integral equations or ray tracing.

Ensuring stability of these hybrid schemes can be very challenging, since stability is a property of the overall scheme, rather than of its individual subsystems. By invoking the concept of dissipation, we can instead achieve stability in an easy and modular way. Each part is seen as an FDTD subsystem and required to satisfy dissipativity conditions (29a)-(29c). Since the connection of dissipative systems is dissipative by construction [17], the overall method will be guaranteed to be stable. The proposed theoretical framework generalizes the so-called energy method [8], and has numerous advantages over the state of the art:

- 1) non-uniform problems can be handled, unlike in the von Neumann analysis [1];
- 2) stability conditions can be given on each subsystem separately, unlike in the iteration method [2], which requires the analysis of the iteration matrix of the whole scheme. This makes stability analysis modular and thus simpler;
- 3) once some given FDTD models have been proven dissipative, they can be arbitrarily interconnected without having to carry out further stability proofs. With the iteration method, when a single part of a coupled scheme changes, the whole proof must be revised;
- 4) the CFL limit of the resulting scheme can be easily determined by applying (37), (38) or (39) to each subsystem and taking the most restrictive CFL limit;
- 5) the stability framework is intuitive, since it is based on the fundamental physical concept of energy dissipation.

IV. APPLICATION: STABLE FDTD SUBGRIDDING

We demonstrate the proposed theory by deriving a subgridding algorithm which is stable by construction, easy to implement and supports an arbitrary grid refinement ratio. The goal is to derive stable update equations for a setup where one or more fine grids are embedded in a main coarse grid. Without loss of generality, we consider the case where a coarse grid with cell size $\Delta x \times \Delta y$ hosts a single fine grid with cell size $\Delta x/r \times \Delta y/r$, where r is an arbitrary integer. The algorithm will ultimately consist of conventional FDTD equations to update the fields that fall strictly inside the two grids, and a special update equation to update the fields on the edges at the grid transition. To derive the method, it is sufficient to consider the interface between a single coarse cell and the corresponding fine cells, as shown in Fig. 2. In the figure a virtual gap has been opened between the two grids for clarity. Without loss of generality, we consider a refinement in the positive x direction. The other three cases can be derived in the same way. The coarse cell under consideration is centered at node $(i + \frac{1}{2}, j - \frac{1}{2})$ and the corresponding fine cells at nodes $(\hat{i} + \frac{1}{2}, \hat{j} + \frac{1}{2}), \dots, (\hat{i} + r - \frac{1}{2}, \hat{j} + \frac{1}{2})$, where coordinates (\hat{i}, \hat{j}) correspond to the same physical location as (i, j) in the coarse grid. Superscript “ $\hat{\cdot}$ ” denotes variables related to the fine grid.

A subgridding algorithm can be interpreted as the result of the connection of the three subsystems, as shown in Fig. 3. Two of those subsystems correspond to the coarse and fine grids to be coupled. The third subsystem represents the interpolation rule which is used to relate the fields on the boundaries of the two grids, that are sampled with different resolution.

A. State Equations for the Coarse and Fine Cells on the Boundary

For the coarse and fine grids, we adopt the formulation of Sec. II, introducing hanging variables on the two boundaries to be connected. The purpose of the hanging variables is to facilitate the coupling of the two meshes and the proof of stability. These extra variables will be eliminated when deriving the update equation for the fields at the interface.

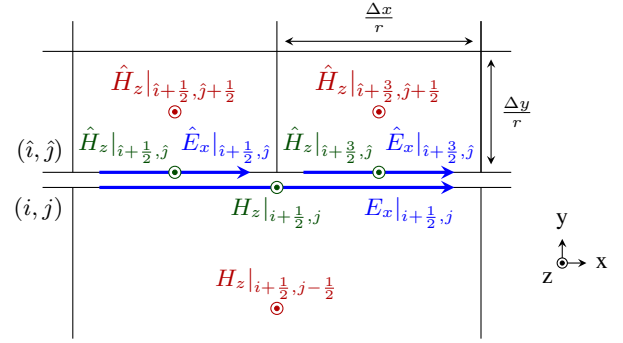


Figure 2: Subgridding scenario considered in Sec. IV for the case of $r = 2$. For clarity, a virtual gap has been inserted between the two grids. This virtual gap is closed when the two grids are connected.

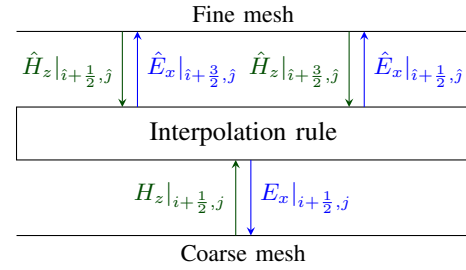


Figure 3: Interpretation of the subgridding method as the connection of three dynamical systems, representing the coarse grid, the fine grid, and the interpolation rule.

On the North boundary of the coarse cell, we introduce the hanging variable

$$H_N^{n+\frac{1}{2}} = H_z|_{i+\frac{1}{2},j}^{n+\frac{1}{2}}. \quad (48)$$

Similarly, on the South fine cell boundaries we introduce the hanging variables

$$\hat{\mathbf{H}}_S^{n+\frac{1}{2}} = \left[\hat{H}_z|_{i+\frac{1}{2},j}^{n+\frac{1}{2}} \quad \dots \quad \hat{H}_z|_{i+r-\frac{1}{2},j}^{n+\frac{1}{2}} \right]^T, \quad (49)$$

as shown in Fig. 2.

From (11), we obtain the following state equation for the coarse E-field sample at the interface and the coarse hanging variable

$$\begin{aligned} \frac{\Delta y}{2} \left(\frac{\varepsilon_x}{\Delta t} + \frac{\sigma_x}{2} \right) E_N^{n+1} = \\ \frac{\Delta y}{2} \left(\frac{\varepsilon_x}{\Delta t} - \frac{\sigma_x}{2} \right) E_N^n + H_N^{n+\frac{1}{2}} - H_{j-\frac{1}{2}}^{n+\frac{1}{2}}, \end{aligned} \quad (50)$$

where

$$H_{j-\frac{1}{2}}^{n+\frac{1}{2}} = H_z|_{i+\frac{1}{2},j-\frac{1}{2}}^{n+\frac{1}{2}}, \quad E_N^n = E_x|_{i+\frac{1}{2},j}^n, \quad (51)$$

and ε_x and σ_x are the permittivity and conductivity on the primary edge of the coarse cell below the interface. Similarly, the state equation for the r fine cells can be written as

$$\begin{aligned} \frac{\Delta y}{2r} \left(\frac{\hat{\mathbf{D}}_{\varepsilon_x}}{\Delta t} + \frac{\hat{\mathbf{D}}_{\sigma_x}}{2} \right) \hat{\mathbf{E}}_S^{n+1} = \\ \frac{\Delta y}{2r} \left(\frac{\hat{\mathbf{D}}_{\varepsilon_x}}{\Delta t} - \frac{\hat{\mathbf{D}}_{\sigma_x}}{2} \right) \hat{\mathbf{E}}_S^n + \hat{\mathbf{H}}_{j+\frac{1}{2}}^{n+\frac{1}{2}} - \hat{\mathbf{H}}_S^{n+\frac{1}{2}}, \end{aligned} \quad (52)$$

where

$$\hat{\mathbf{H}}_{j+\frac{1}{2}}^{n+\frac{1}{2}} = \left[\hat{H}_z|_{i+\frac{1}{2}, j+\frac{1}{2}}^{n+\frac{1}{2}} \quad \cdots \quad \hat{H}_z|_{i+r-\frac{1}{2}, j+\frac{1}{2}}^{n+\frac{1}{2}} \right]^T, \quad (53)$$

$$\hat{\mathbf{E}}_S^n = \left[\hat{E}_x|_{i+\frac{1}{2}, j}^n \quad \cdots \quad \hat{E}_x|_{i+r-\frac{1}{2}, j}^n \right]^T, \quad (54)$$

and $\hat{\mathbf{D}}_{\varepsilon_x}$ and $\hat{\mathbf{D}}_{\sigma_x}$ are $r \times r$ diagonal matrices containing the values of permittivity and conductivity above the interface for the South edges where the fine \hat{E}_x fields are sampled.

B. Interpolation Rule

The interpolation rule [29] relates the field sampled on the coarse and fine grids. From the boundary condition for tangential electric fields, we have that

$$\hat{\mathbf{E}}_S^n = E_N^n \mathbf{T} \quad \forall n, \quad (55)$$

where \mathbf{T} is an $r \times 1$ matrix of ones. Condition (55) forces the coarsely- and finely-sampled E fields to be equal at all times.

On the magnetic fields at the boundary, we impose a constraint reciprocal to (55)

$$H_N^{n+\frac{1}{2}} = \frac{\mathbf{T}^T \hat{\mathbf{H}}_S^{n+\frac{1}{2}}}{r} \quad \forall n. \quad (56)$$

We will see in Sec. IV-D that the reciprocity between the E and H interpolation rules is required to ensure stability.

C. Explicit Update Equation for the Interface

Interpolation conditions (55) and (56) can now be used to combine (50) and (52) in order to derive an explicit update equation for the fields at the coarse-fine interface, and eliminate hanging variables.

Substituting (55) into (52), and multiplying the obtained equation by \mathbf{T}^T/r on the left yields

$$\begin{aligned} \frac{\Delta y}{2r} \left(\frac{\mathbf{T}^T \hat{\mathbf{D}}_{\varepsilon_x} \mathbf{T}}{r \Delta t} + \frac{\mathbf{T}^T \hat{\mathbf{D}}_{\sigma_x} \mathbf{T}}{2r} \right) E_N^{n+1} = \\ \frac{\Delta y}{2r} \left(\frac{\mathbf{T}^T \hat{\mathbf{D}}_{\varepsilon_x} \mathbf{T}}{r \Delta t} - \frac{\mathbf{T}^T \hat{\mathbf{D}}_{\sigma_x} \mathbf{T}}{2r} \right) E_N^n \\ + \frac{\mathbf{T}^T \hat{\mathbf{H}}_{j+\frac{1}{2}}^{n+\frac{1}{2}}}{r} - \frac{\mathbf{T}^T \hat{\mathbf{H}}_S^{n+\frac{1}{2}}}{r}. \end{aligned} \quad (57)$$

For the simplicity of notation we define symbols for the average permittivity and conductivity of the r South boundary fine cells

$$\hat{\varepsilon}_x = \frac{\mathbf{T}^T \hat{\mathbf{D}}_{\varepsilon_x} \mathbf{T}}{r}, \quad \hat{\sigma}_x = \frac{\mathbf{T}^T \hat{\mathbf{D}}_{\sigma_x} \mathbf{T}}{r}. \quad (58)$$

Equation (57) can now be added to (50), yielding

$$\begin{aligned} \frac{\Delta y}{2} \left(\frac{\varepsilon_x + \frac{\hat{\varepsilon}_x}{r}}{\Delta t} + \frac{\sigma_x + \frac{\hat{\sigma}_x}{r}}{2} \right) E_N^{n+1} = \\ \frac{\Delta y}{2} \left(\frac{\varepsilon_x + \frac{\hat{\varepsilon}_x}{r}}{\Delta t} - \frac{\sigma_x + \frac{\hat{\sigma}_x}{r}}{2} \right) E_N^n \\ + H_N^{n+\frac{1}{2}} - H_{j-\frac{1}{2}}^{n+\frac{1}{2}} + \frac{\mathbf{T}^T \hat{\mathbf{H}}_{j+\frac{1}{2}}^{n+\frac{1}{2}}}{r} - \frac{\mathbf{T}^T \hat{\mathbf{H}}_S^{n+\frac{1}{2}}}{r}. \end{aligned} \quad (59)$$

With the interpolation rule (56), we cancel the hanging variables to obtain

$$\begin{aligned} \frac{\Delta y}{2} \left(\frac{\varepsilon_x + \frac{\hat{\varepsilon}_x}{r}}{\Delta t} + \frac{\sigma_x + \frac{\hat{\sigma}_x}{r}}{2} \right) E_N^{n+1} = \\ \frac{\Delta y}{2} \left(\frac{\varepsilon_x + \frac{\hat{\varepsilon}_x}{r}}{\Delta t} - \frac{\sigma_x + \frac{\hat{\sigma}_x}{r}}{2} \right) E_N^n - H_{j-\frac{1}{2}}^{n+\frac{1}{2}} + \frac{\mathbf{T}^T \hat{\mathbf{H}}_{j+\frac{1}{2}}^{n+\frac{1}{2}}}{r}. \end{aligned} \quad (60)$$

Rearranging (60), we get the following *explicit* update equation for E_N in terms of the neighboring magnetic fields

$$\begin{aligned} E_N^{n+1} = \left(\frac{\varepsilon_x + \frac{\hat{\varepsilon}_x}{r}}{\Delta t} + \frac{\sigma_x + \frac{\hat{\sigma}_x}{r}}{2} \right)^{-1} \left(\frac{\varepsilon_x + \frac{\hat{\varepsilon}_x}{r}}{\Delta t} - \frac{\sigma_x + \frac{\hat{\sigma}_x}{r}}{2} \right) E_N^n \\ + \frac{2}{\Delta y} \left(\frac{\varepsilon_x + \frac{\hat{\varepsilon}_x}{r}}{\Delta t} + \frac{\sigma_x + \frac{\hat{\sigma}_x}{r}}{2} \right)^{-1} \left(\frac{\mathbf{T}^T \hat{\mathbf{H}}_{j+\frac{1}{2}}^{n+\frac{1}{2}}}{r} - H_{j-\frac{1}{2}}^{n+\frac{1}{2}} \right). \end{aligned} \quad (61)$$

The fine interface electric fields are then updated using (55). It should be noted that, when $r = 1$, equation (61) reduces to the standard FDTD update equation.

The overall subgridding algorithm can be summarized as follows:

- 1) Calculate the magnetic field samples everywhere at time $n + \frac{1}{2}$ using conventional FDTD update equations.
- 2) Use standard FDTD update equations to compute the E fields at time $n + 1$ on the edges that are strictly inside the coarse and fine grids.
- 3) Compute E_N^{n+1} , the coarsely-sampled electric field at the interface, using (61).
- 4) Update the finely-sampled \hat{E}_x fields at the interface using (55).

The computational overhead of this scheme is minimal, since the coefficients in (61) can be pre-computed before the update iterations.

The proposed method is thus simple to implement, since it consists of conventional FDTD update equations inside the two meshes and a modified update equation for the edges at the interface. In comparison to previous subgridding methods, we avoid non-rectangular cells [6], finite element concepts [20] and Withney forms [21], [22]. The proposed update equation can be also used at corners with no modifications, unlike in previous works that require special treatment [5] or L-shaped cells [6]. Finally, we remark that in Sec. II, the FDTD update equations have been given in matrix form in order to reveal the dissipative nature of FDTD systems. This form, however, does not have to be used in the practical implementation, which can use conventional for loops or, in languages like MATLAB, vectorized operations.

D. Proof of Stability

The proposed dissipation theory makes it straightforward to prove that the subgridding algorithm is stable under the CFL limit of the fine grid. For stability, all three subsystems in Fig. 3 need to be dissipative, which requires one to use the

more restrictive fine grid time step. With the time step chosen correctly, in order to guarantee the overall stability we need to only ensure dissipativity of the interpolation rule.

Analogously to (23) the supply rate for the interpolation subsystem is defined as

$$s(\mathbf{y}^n, \mathbf{u}^{n+\frac{1}{2}}) = -\Delta t \Delta x \frac{E_N^n + E_N^{n+1}}{2} H_N^{n+\frac{1}{2}} + \Delta t \frac{\Delta x}{r} \frac{(\hat{\mathbf{E}}_S^n + \hat{\mathbf{E}}_S^{n+1})^T}{2} \hat{\mathbf{H}}_S^{n+\frac{1}{2}}. \quad (62)$$

Substituting (55) and (56) into (62), we have

$$s(\mathbf{y}^n, \mathbf{u}^{n+\frac{1}{2}}) = \Delta t \Delta x \frac{(E_N^n + E_N^{n+1})^T}{2} \left(\frac{\mathbf{T}^T \hat{\mathbf{H}}_S^{n+\frac{1}{2}}}{r} - H_N^{n+\frac{1}{2}} \right) = 0. \quad (63)$$

Therefore, the proposed interpolation rule is a lossless system that does not dissipate nor absorb any energy. Physically, this result makes sense, since the connection system corresponds to an infinitely thin region where no energy dissipation can take place. In conclusion, since the proposed subgridding method can be seen as the connection of three dissipative systems, it is overall dissipative, and thus stable.

V. NUMERICAL EXAMPLES

The following sections provide the results of FDTD simulations that were done to verify the proposed theory. The subgridding algorithm was implemented in Matlab and tests were performed in order to check its stability, ability to handle material traverse, its accuracy and speedup capability.

A. Stability Verification

Stability was verified by simulating an empty cavity with perfect electric conductor (PEC) walls with a centrally placed subgridding region for 10^6 time steps. The layout of the simulation is shown in Fig. 4. The cavity was excited using a modulated Gaussian magnetic current source with central frequency of 3.75 GHz and half-width at half-maximum of 0.74 GHz. Magnetic field was recorded at a probe placed inside the cavity. The time step was set 1% below the CFL limit of the fine grid.

The resulting waveform in Fig. 5 shows that no instability occurred after 10^6 time steps. Stable behavior after such a large number of time steps verifies the correctness of the proposed stability enforcement technique, especially since no lossy materials were present to dissipate any spurious energy artificially created by the algorithm.

B. Material Traverse

The ability of the proposed method to produce meaningful results when objects traverse the subgridding interface was tested using the setup in Fig. 6. A 16×16 mm slab of material was simulated for three different placements of the subgridding region: enclosing, traversing and away from the slab. The test was done for copper and a lossy dielectric with conductivity of 5 S/m and relative permittivity of 2.

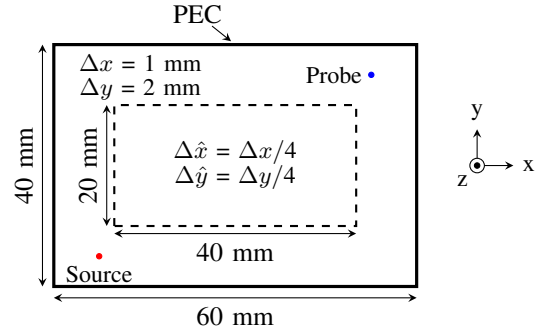


Figure 4: Layout of the PEC cavity considered in Sec. V-A.

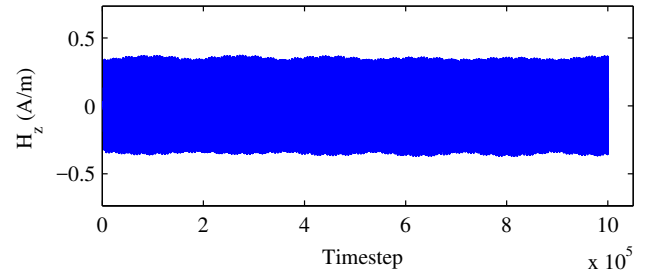


Figure 5: Magnetic field at the probe for the the empty cavity with subgridding of Sec. V-A, computed for 10^6 time steps.

As a reference, uniformly discretized all-coarse and all-fine simulations were performed at the fine time step, in addition to the subgridding simulations. Coarse and fine meshes in uniformly discretized and subgridding runs were chosen as 1 mm and 0.2 mm respectively. 15 mm-thick perfectly matched layer (PML) terminated the simulation region. Modulated Gaussian magnetic current excitation was used at 15.0 GHz central frequency with 8.82 GHz half-width at half-maximum bandwidth. The time step was chosen as 0.467 ps in all test cases.

The magnetic field waveforms at the probe recorded in the different subgridding scenarios are shown in Fig. 7, and are in excellent agreement among each other. This result confirms that the proposed subgridding method can properly handle material traverse, for both very good conductors and for lossy dielectrics.

C. Application to Simulating Scatterer Reflections

In order to investigate the accuracy of the proposed scheme, we looked at waveguide reflections from the scatterer shown in Fig. 8, which consisted of four copper rods with 1 mm radius. We have also investigated the reflections from the subgridding interface, in order to assess the quality of the subgridding scheme. The coarse cell was chosen to be 1 mm, which was $\frac{1}{10}$ of the minimum wavelength of interest that corresponded to 30.0 GHz. The fields of the incident wave were computed by running a reference simulation without the scatterer and without subgridding. Reflected wave fields were found by subtracting the incident wave fields from the total fields in simulations with the scatterer. 15 mm-thick PML boundary was chosen to terminate the two sides of the waveguide. The

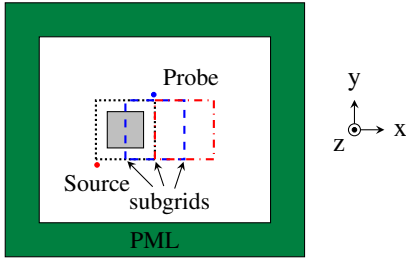


Figure 6: Layout used for the material traverse test of Sec. V-B, and the three different placements of the subgridding region.

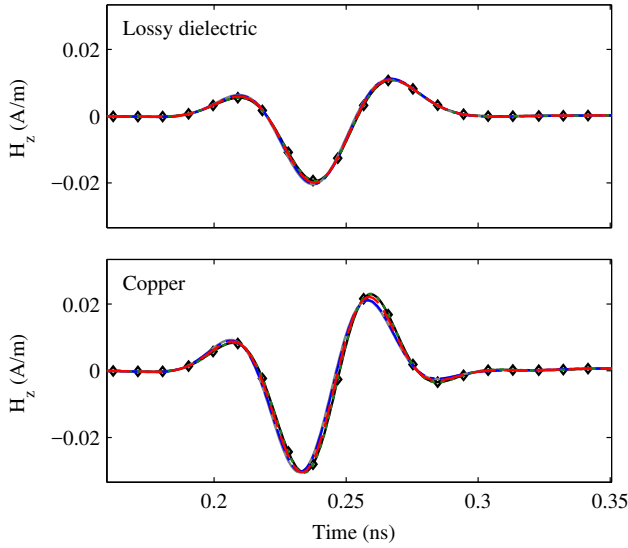


Figure 7: Time-domain magnetic field at the probe recorded for the three locations of the subgrid in Sec. V-B: enclosed (---), outside (---) and traversing the object (---). Waveforms from the uniformly discretized all-coarse (—◇—) and all-fine (—) simulations are also shown.

time steps in the subgridding runs were set 1% below the CFL limit of the refined region. Uniformly discretized simulations were run 1% below the CFL limits of the respective grids.

The resulting reflections are shown in Fig. 9 for the subgridding case with different refinement ratios, as well as the reference run with full refinement by a factor of 6. The simulation times are shown in Table I. It can be seen that the local refinement of the grid around the scatterer with the proposed subgridding method can improve the accuracy substantially compared to the coarse grid run. The larger choice of refinement ratio makes the solution very close to the reference all-fine solution. Moreover, very good speedup - almost by a factor of 11 - is achieved even for the grid refinement of 6 when the redundant high resolution of the grid in air is eliminated. The reflections from subgridding interface were significantly lower than those from the scatterer, further demonstrating the accuracy of the proposed method.

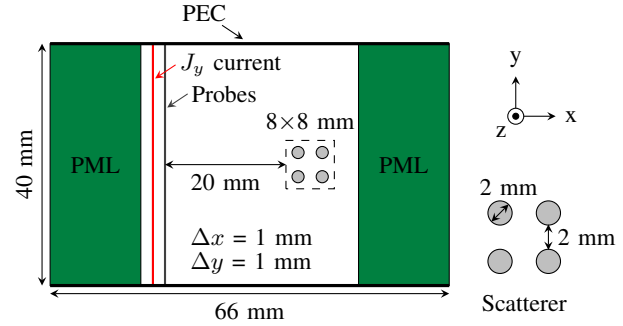


Figure 8: Layout of the four-rod reflection simulation discussed in Sec. V-C. The dashed line shows the location of the subgrid in the subgridding run.

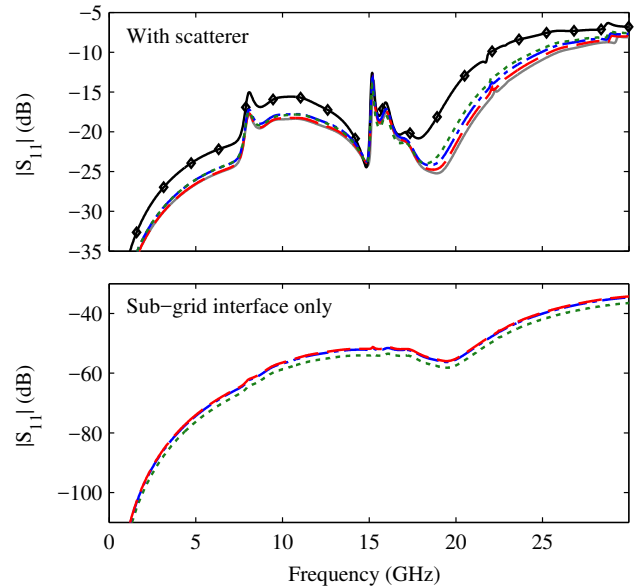


Figure 9: Reflected power with respect to the incident for the example of Sec. V-C. Top panel: reflections from the four-rod scatterer for different global discretization: all-coarse (—◇—) and all-fine with $r = 6$ (—); and for the subgridding runs: $r = 2$ (---), $r = 4$ (---) and $r = 6$ (---). Bottom panel: reflections from the subgrid interface only.

D. Application to Exposure Studies

We show the possibility of applying the method for multi-scale human exposure simulations. The chosen setup is shown in Fig. 10. A transverse cross-section of the head of the model of Ella from IT'IS Virtual Population V1.x [30] was used to assign the material properties [31] to the FDTD cells. A 900 MHz source was placed approximately 3 meters away from the human head. The simulation region was terminated with 20 cm PML. The reference (fine) resolution in the tissues was set to 2 mm, based on the mesh size chosen by [32] in a radiation exposure study at that frequency. Specific absorption rate, or SAR, was evaluated according to the formula in [33], which was used as follows for sinusoidal excitation

$$SAR = \frac{\sigma(E_{x_p}^2 + E_{y_p}^2)}{2\rho}, \quad (64)$$

Table I: Simulation times for different meshes in four-rod scatterer simulations in Sec. V-C. Simulation times were recorded for the total field run only - not for the reference run.

Method	Simulation time (s)
All-fine ($r = 6$)	427.4
All-coarse	3.2
Subgridding ($r = 2$)	10.7
Subgridding ($r = 4$)	23.3
Subgridding ($r = 6$)	39.5

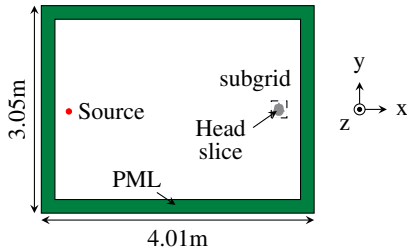


Figure 10: Layout of the simulation in Sec. V-D with human head cross-section placed approximately 3 meters away from a point source.

where subscript “ p ” denotes the peak absolute value of a field component and ρ corresponds to tissue density. SAR was calculated for each of the primary cells. The values of the electric field components at the primary cell centers were found by averaging the nearest known samples at the cell edges. The peak values of the fields were found for the time interval from 25.6 ns to 26.8 ns, which gave the wave sufficient time to reach the head and penetrate inside it.

In the subgridding run, the empty space was coarsened to 1 cm, which corresponded to $\frac{1}{33.3}$ of the wavelength. The reference all-fine run was performed at 2 mm resolution, along with the all-coarse run where the entire simulation region was discretized at 1 cm. The volumetric integral of SAR over the tissues was used as an accuracy metric

$$\sum_i \sum_j SAR|_{i+\frac{1}{2}, j+\frac{1}{2}} \Delta x \Delta y, \quad (65)$$

where Δx and Δy are FDTD cell dimensions in the tissues. Time step of 4.67 ps was chosen for the all-fine simulation and for the subgridding simulation. The coarse grid case was run at 23.11 ps.

The resulting SAR maps are shown in Fig. 11. Table II shows simulation times and percent error in the total SAR with respect to the all-fine simulation. The results show that with subgridding a speedup of 46X can be obtained with only 3.1% loss in accuracy. No noticeable difference can be seen on the SAR maps in Fig. 11 between the subgridding and all-fine simulations. When, instead, the coarse resolution was chosen for the entire grid, the head tissues were not sufficiently resolved and the integral SAR differed from the reference by 59.5%, showing the necessity of local grid refinement.

VI. CONCLUSION

This paper proposed a dissipative systems theory for FDTD, recognizing that FDTD equations can be seen as a dynamical

Table II: Error in the integral of SAR and simulation times in the simulations discussed in Sec. V-D.

Method	Error in SAR integral	Simulation time (s)
All-fine	Not applicable	1596.4
All-coarse	59.5%	6.9
Subgridding	-3.1%	34.5

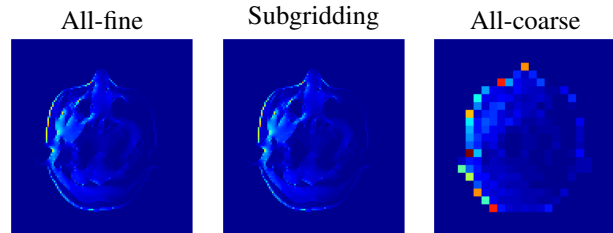


Figure 11: SAR maps obtained in Sec. V-D with all-fine (2 mm), all-coarse (1 cm) discretization and with subgridding (2 mm in the tissues and 1 cm in the air).

system which is dissipative under a generalized Courant-Friedrichs-Lewy condition. The theory provides a new, powerful framework to make FDTD stability analysis simpler and modular. Stability conditions can indeed be given on the individual components (e.g. boundary conditions, meshes, thin-wire models) rather than on the whole coupled FDTD setup. The theory is intuitive since rooted on the familiar concept of energy dissipation, and sheds new light on the root mechanisms behind FDTD instability. As an example of application, a simple yet effective subgridding algorithm is derived, with straightforward stability proof. The proposed algorithm allows material traverse, is simpler to implement than existing solutions, and supports an arbitrary grid refinement ratio. Numerical results confirm its stability and accuracy. Speedups of up to 46X were observed with only 3.1% error with respect to standard FDTD.

REFERENCES

- [1] A. Taflov and S. C. Hagness, *Computational electrodynamics*. Artech house, 2005.
- [2] S. D. Gedney, *Introduction to the Finite-Difference Time-Domain (FDTD) Method for Electromagnetics*, 1st ed. San Rafael, CA: Morgan & Claypool Publishers, 2011.
- [3] K. Yee, “Numerical solution of initial boundary value problems involving Maxwell’s equations in isotropic media,” *IEEE Trans. Antennas Propag.*, vol. 14, no. 3, pp. 302–307, 1966.
- [4] M. Okoniewski, E. Okoniewska, and M. Stuchly, “Three-dimensional subgridding algorithm for FDTD,” *IEEE Trans. Antennas Propag.*, vol. 45, no. 3, pp. 422–429, 1997.
- [5] P. Thoma and T. Weiland, “A consistent subgridding scheme for the finite difference time domain method,” *Int. J. Numer. Model. EL.*, vol. 9, no. 5, pp. 359–374, 1996.
- [6] K. Xiao, D. J. Pommerenke, and J. L. Drewniak, “A three-dimensional FDTD subgridding algorithm with separated temporal and spatial interfaces and related stability analysis,” *IEEE Trans. Antennas Propag.*, vol. 55, no. 7, pp. 1981–1990, 2007.
- [7] W. Sui, D. A. Christensen, and C. H. Durney, “Extending the two-dimensional FDTD method to hybrid electromagnetic systems with active and passive lumped elements,” *IEEE Trans. Microw. Theory Techn.*, vol. 40, no. 4, pp. 724–730, 1992.
- [8] F. Edelvik, R. Schuhmann, and T. Weiland, “A general stability analysis of FIT/FDTD applied to lossy dielectrics and lumped elements,” *International Journal of Numerical Modelling: Electronic Networks, Devices and Fields*, vol. 17, no. 4, pp. 407–419, 2004.

- [9] B. Denecker, F. Olyslager, L. Knockaert, and D. De Zutter, "Generation of FDTD subcell equations by means of reduced order modeling," *IEEE Trans. Antennas Propag.*, vol. 51, no. 8, pp. 1806–1817, 2003.
- [10] X. Li, C. D. Sarris, and P. Triverio, "Structure-Preserving Reduction of Finite-Difference Time-Domain Equations with Controllable Stability Beyond the CFL Limit," *IEEE Trans. Microw. Theory Techn.*, vol. 62, no. 12, pp. 3228–3238, 2014.
- [11] X. Li and P. Triverio, "Stable FDTD Simulations with Subgridding at the Time Step of the Coarse Grid: a Model Order Reduction Approach," in *IEEE MTT-S Int. Conf. on Numerical Electromagnetic and Multiphysics Modeling and Optimization*, Ottawa, Canada, August 11–14 2015.
- [12] J.-F. Lee, R. Lee, and A. Cangellaris, "Time-domain finite-element methods," *IEEE Trans. Antennas Propag.*, vol. 45, no. 3, pp. 430–442, 1997.
- [13] A. R. Bretones, R. Mittra, and R. G. Martín, "A hybrid technique combining the method of moments in the time domain and FDTD," *IEEE Microw. Guided Wave Lett.*, vol. 8, no. 8, pp. 281–283, 1998.
- [14] Y. Wang, S. Safavi-Naeini, and S. K. Chaudhuri, "A hybrid technique based on combining ray tracing and FDTD methods for site-specific modeling of indoor radio wave propagation," *IEEE Trans. Antennas Propag.*, vol. 48, no. 5, pp. 743–754, 2000.
- [15] T. Namiki, "A new FDTD algorithm based on alternating-direction implicit method," *IEEE Microw. Wireless Compon. Lett.*, vol. 47, no. 10, pp. 2003–2007, 1999.
- [16] F. Zheng, Z. Chen, and J. Zhang, "A Finite-Difference time-domain method without the Courant stability conditions," *IEEE Microwave Guided Wave Lett.*, vol. 9, no. 11, pp. 441–443, Nov 1999.
- [17] P. Triverio, S. Grivet-Talocia, M. S. Nakhla, F. Canavero, R. Achar, "Stability, causality, and passivity in electrical interconnect models," *IEEE Trans. Adv. Packag.*, vol. 30, no. 4, pp. 795–808, 2007.
- [18] J. C. Willems, "Dissipative dynamical systems part i: General theory," *Archive for rational mechanics and analysis*, vol. 45, no. 5, pp. 321–351, 1972.
- [19] Y. Wang, S. Langdon, and C. Penney, "Analysis of accuracy and stability of FDTD subgridding schemes," in *2010 European Microwave Conf. IEEE*, 2010, pp. 1297–1300.
- [20] F. Collino, T. Fouquet, and P. Joly, "Conservative space-time mesh refinement methods for the FDTD solution of Maxwell's equations," *J. Comput. Phys.*, vol. 211, no. 1, pp. 9–35, 2006.
- [21] R. A. Chilton and R. Lee, "Conservative and provably stable FDTD subgridding," *IEEE Trans. Antennas Propag.*, vol. 55, no. 9, pp. 2537–2549, 2007.
- [22] N. V. Venkatarayalu, R. Lee, Y.-B. Gan, and L.-W. Li, "A stable FDTD subgridding method based on finite element formulation with hanging variables," *IEEE Trans. Antennas Propag.*, vol. 55, no. 3, pp. 907–915, 2007.
- [23] J. Brewer, "Kronecker products and matrix calculus in system theory," *IEEE Trans. Circuits Syst.*, vol. 25, no. 9, pp. 772–781, 1978.
- [24] B. Denecker, F. Olyslager, L. Knockaert, and D. De Zutter, "A new state-space-based algorithm to assess the stability of the Finite-Difference time-domain method for 3D finite inhomogeneous problems," *AEU-Int. J. Electron. C.*, vol. 58, no. 5, pp. 339 – 348, 2004.
- [25] L. Dai, "Singular control systems," 1989.
- [26] C. Byrnes and W. Lin, "Losslessness, feedback equivalence, and the global stabilization of discrete-time nonlinear systems," *IEEE Trans. Autom. Control*, vol. 39, no. 1, pp. 83–98, 1994.
- [27] S. Grivet-Talocia and B. Gustavsen, *Passive Macromodeling: Theory and Applications*. Hoboken, NJ: Wiley, 2015.
- [28] S. Boyd, L. El Ghaoui, E. Feron, and V. Balakrishnan, *Linear Matrix Inequalities in System and Control Theory*, ser. Studies in Applied Mathematics. SIAM, 1994, vol. 15.
- [29] L. Kulas and M. Mrozowski, "Reciprocity principle for stable subgridding in the finite difference time domain method," in *EUROCON, 2007. The International Conference on "Computer as a Tool"*, Sept 2007, pp. 106–111.
- [30] A. Christ *et al.*, "The Virtual Family - Development of surface-based anatomical models of two adults and two children for dosimetric simulations," *Physics in Medicine and Biology*, vol. 55, no. 2, pp. N23–N38, 2010.
- [31] IT'IS Foundation, "Overview - Database of Tissue Properties." [Online]. Available: <http://www.itis.ethz.ch/virtual-population/tissue-properties/overview/> [Aug. 19, 2015].
- [32] S. Kühn *et al.*, "MMF/GSMA phase 2: scientific basis for base station exposure compliance standards," IT'IS Foundation, Tech. Rep. 21, June 2009.
- [33] D. A. Sánchez-Hernández, *High Frequency Electromagnetic Dosimetry*. Boston, MA: Artech House, 2009.